

A Phase Camera for Advanced Virgo

MITA TEMBE

University of Virginia
National Institute for Subatomic Physics (Nikhef)

12 August 2014

Abstract

A phase camera is a frequency-selective wave front sensor. Operating on the principle of optical heterodyne detection, it will be used at three ports of the Advanced Virgo interferometer to monitor and control aberrations in the test mirrors. The experimental phase camera setup at Nikhef provides an opportunity to gauge effectiveness of the phase camera and solve any issues with operation before installing cameras at Advanced Virgo. In order to obtain large power for the heterodyne (reference) beam, an optimization of the injection beam and its conditions were studied. Subsequently, optical layouts for the three phase cameras were created and will soon be implemented at Virgo.

I. INTRODUCTION

I. Gravitational Waves

First predicted by Albert Einstein in 1916, gravitational waves form an integral part of Einstein's theory of general relativity. This theory states that gravity is a characteristic of the curvature of space-time. Mass and energy affect the magnitude of this curvature. Accelerating masses create gravitational waves, tiny ripples in space-time that emanate from the source at the speed of the light. In order for these gravitational waves to be observed, extremely large masses must be involved. For example, the coalescences of black holes and neutron stars, pulsars, and supernova explosions will serve as sources of gravitational waves. As of now, gravitational waves have not yet been directly detected, leaving only one remaining piece of Einstein's immensely successful theory to be proven.

II. Gravitational Wave Detectors

Gravitational wave detectors currently take the form of large Michelson interferometers, located in several places around the world. The next generation of detectors currently being commissioned include Advanced LIGO in Louisiana and Washington; Advanced Virgo in Cascina, Italy; and KAGRA in Japan. Advanced Virgo is a Michelson interferometer with 3 km long arms. Its design contains a power recycling cavity and a signal recycling cavity, both of which are currently being prepared. The commissioning of Advanced Virgo will result in an increase of sensitivity of one order of magnitude over Virgo, corresponding to an increase of three orders of magnitude in the volume of the universe capable of being observed. This increase in sensitivity will create significantly more opportunities per year for observing GW events.

III. Phase Camera

The phase camera, a frequency selective wave front sensor, will serve as a monitor for the aberrations of the test mirrors in the Michelson interferometer at Advanced Virgo. It operates

on the main principles of heterodyne detection and pinhole scanning. A brief summary of the operation of the phase camera is as follows: the incoming laser beam is split into two parts: a test beam and a reference beam. The test beam passes through the actual interferometer, while the reference beam is shifted in frequency; the two beams are then recombined. The combined beam is scanned across a pinhole attached to a photodetector, which detects the beat signal between the test and reference beams (heterodyne detection).

The phase camera will be placed at three ports of the interferometer: the input port (PC1), at the power recycling cavity (PC2), and the output port (PC3). PC2 will be connected to the Thermal Compensation System (TCS) to compensate for mirror aberrations, while PC1 and PC3 will serve as monitoring sensors.

II. PHASE CAMERA

I. Operation

The phase camera consists of several different components: a laser, beam splitters, an Electro-Optic Modulator (EOM), an Acousto-Optic Modulator (AOM), collimators, lenses, mirrors, a scanner, and a photodetector (PD). The experimental setup at Nikhef can be seen below:

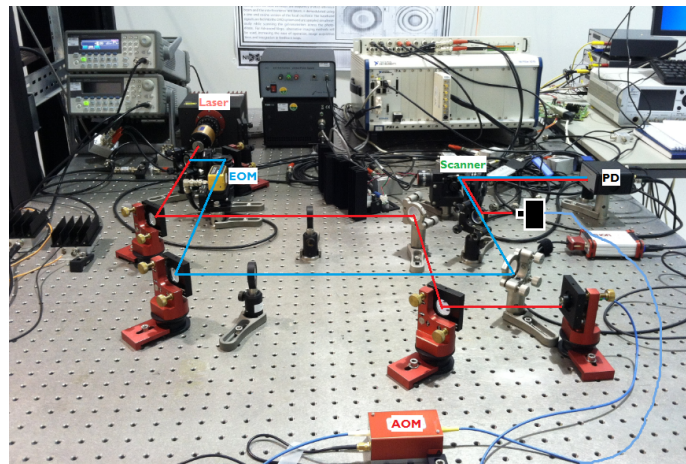


Figure 1: Final setup for the phase camera at Nikhef

The laser used in the experimental setup at Nikhef is a 500 mW, 1064 nm laser. The laser passes through a Faraday isolator to prevent the beam from reflecting backwards, then through a beam splitter, which splits the beam into two equal beams of half-power (250 mW). One beam passes through the EOM, which phase-modulates the beam and creates sidebands. These sidebands are portions of the modulated carrier wave, which are both above or below the carrier wave. In this experiment, we used a single sideband. However, in Advanced Virgo there will be 5 sidebands, as can be seen in Figure 2. The beam that passes through the EOM becomes the test beam, which then passes through the interferometer.

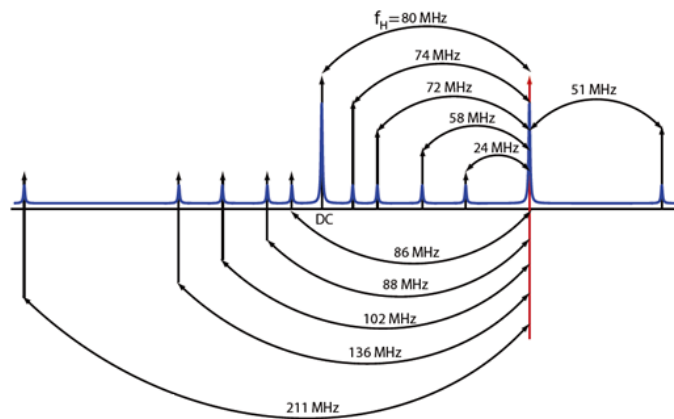


Figure 2: Five sidebands to be used in Advanced Virgo^[2]

The other beam passes through the AOM, which frequency-shifts the beam by 80 MHz. Within the AOM, an oscillating signal drives a transducer to vibrate, creating sound waves. These sound waves create alternating areas of high and low density, due to the longitudinal nature of sound waves, which in turn alters the index of refraction within the AOM. These planes of alternating index of refraction result in Bragg scattering of the input beam and a frequency shift of 80 MHz.

The test beam and reference beam are then recombined with another beam splitter and scanned across a pinhole of typical aperture size of 5 mm, and directed into the PD. The beam signals are then mapped in both amplitude and phase, creating the maps in Figure 3.

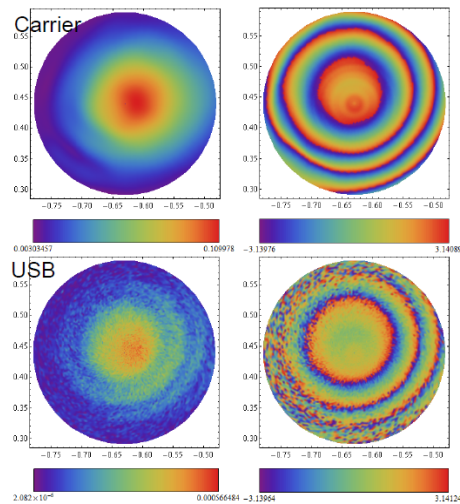


Figure 3: Amplitude (left) and phase (right) maps for the carrier and upper sideband^[4]

In an ideal interferometer, the phase maps of the carrier and sideband should be identical, so by subtracting the two, we can find a map of the actual mirror aberrations. In the case of PC2, this information will be fed to a CO₂ laser which will compensate for the mirror distortions, by working with the Thermal Compensation System (TCS).

II. Goals

There were two main goals for this project. The first was to find the source of an 86 percent power loss through the AOM and improve the power transmission, in order to increase the signal-to-noise ratio of the system. The AOM specification sheet predicts a maximum loss of 37 percent, significantly smaller than the measured transmission ratio.

The second goal was to create optical layout diagrams for the three phase cameras at the Advanced Virgo site.

III. GOAL 1: IMPROVE POWER TRANSMISSION

I. Initial Conditions

Figure 4 depicts the initial setup of the reference beam portion of the phase camera, with the numbers denoting values in centimeters. In this project, only the reference beam portion of the phase camera was studied, as the power loss occurred through the AOM.

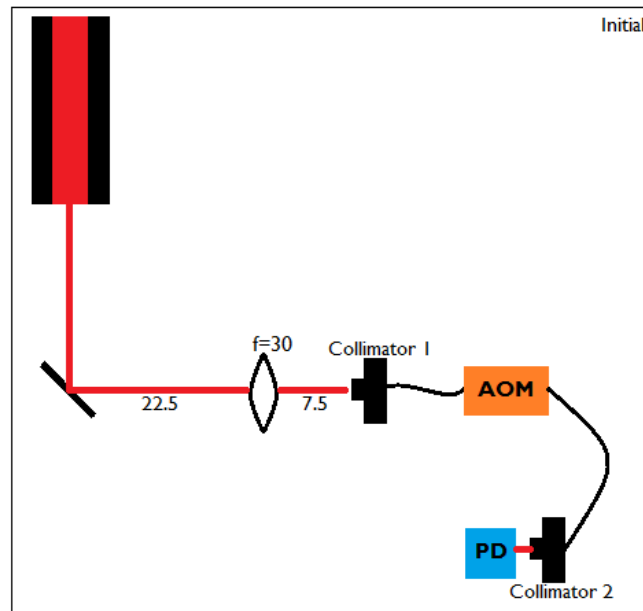


Figure 4: Initial setup of the reference beam portion of the phase camera

Initial measurements of the power at Collimator 1 and Collimator 2 revealed that there was an 86 percent loss in power as the laser beam traveled through the AOM. The input power was 250 mW, as expected with a beam splitter halving the 500 mW beam, while the output power at Collimator 2 was only 36 mW. It should be noted that these values were measured using an incorrect calibration on the powermeter software of a wavelength of 635 nm, instead of 1064 nm. This mistake was rectified and accounted for later in the experiment. However, the ratio of power loss is preserved.

We postulated two reasons for the loss: (1) poor mode-matching between the input beam and Collimator 1, and (2) a non-optimized voltage of the AOM. We proposed to test both these hypotheses and attempt to improve the power transmission.

II. Mode Matching

Mode matching is a method of matching a laser beam to an optical fiber or resonant cavity, in order to create efficient coupling[6]. This technique can be used to determine the focal lengths and positions of one or more lenses to be placed in the beam in order to mode match two beams.

Passing a Gaussian beam, defined as a beam whose intensity and electric field distributions vary in a Gaussian manner, through some sort of optical element changes the waist size and waist position of the beam. It is this change in waist size and position which we intended to utilize to improve the mode matching. The calculations required stem from the use of ABCD matrices, or ray analysis matrices, which detail the effect an optical element has on a Gaussian beam. These matrices are 2×2 matrices, which differ for each optical element. In this experiment, we used the matrix for a thin lens, shown below, where f is the focal length[5]:

$$\begin{bmatrix} 1 & 0 \\ -\frac{1}{f} & 1 \end{bmatrix} \quad (1)$$

Using this matrix to describe our system resulted in the following four equations[3], which were used several times to determine the optimal lens locations.

$$M = \frac{w_{0out}}{w_{0in}} \quad (2)$$

$$f_0 = \frac{\pi w_{0in} w_{0out}}{\lambda} \quad (3)$$

$$d_{in} = f \pm \frac{1}{M} \sqrt{f^2 - f_0^2} \quad (4)$$

$$d_{out} = f \pm M \sqrt{f^2 - f_0^2} \quad (5)$$

M refers to the magnification of the beam, or the ratio between output and input waist sizes. The value f_0 refers to the minimum value of the lens focal length necessary in order to mode match two beams. The values d_{in} and d_{out} are the distances between the input waist and lens and the lens and output waist, respectively, and determine the actual physical setup of the optical elements. This can be seen in Figure 5:

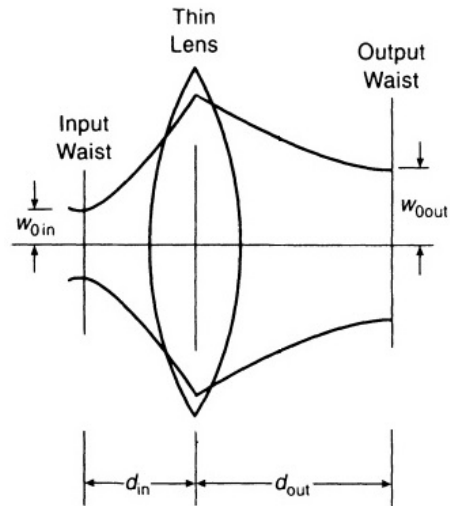


Figure 5: Positions of input and output waists in relation to lens^[5]

In order to use these four equations, measurements of the beam waists and positions were required. To find these values, we measured beam profiles, which is the width of a laser beam as a function of distance along its optical axis. We used two different beam profilers to perform these measurements in different power ranges. Beam profiles of the input beam and Collimator 1 were measured, and Collimator 2 was measured previously. The beam profiler was set up as close to the source of the beam as possible, and then moved by equal increments (1 or 2 cm) to take measurements in both horizontal and vertical transverse directions of the beam. Figures ^[6] and ^[7] show the position of the beam profiler in relation to the other components.

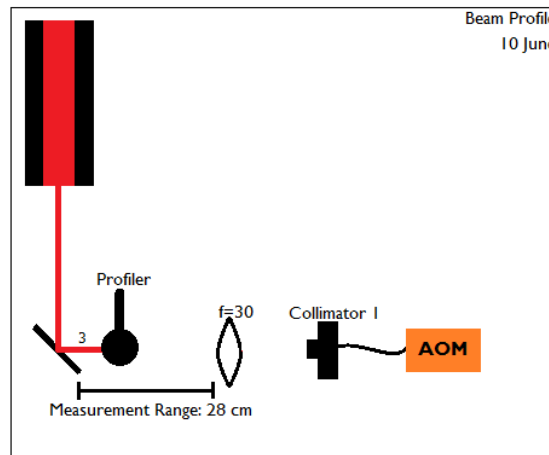


Figure 6: Position of the beam profiler when measuring the input beam

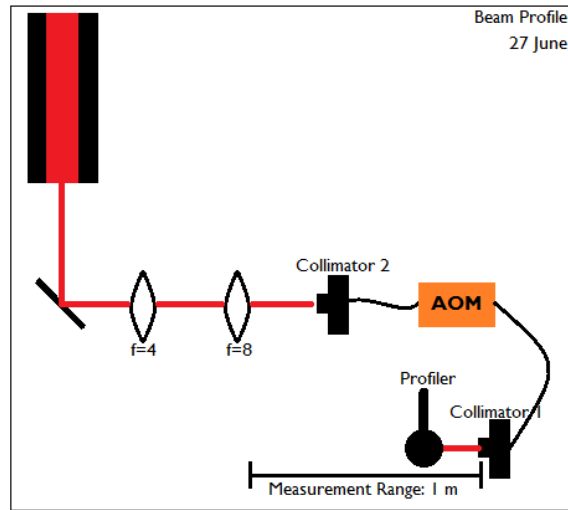


Figure 7: Position of the beam profiler when measuring Collimator 1

In order to measure the beam profile of Collimator 1, the positions of Collimators 1 and 2 were switched. Two lenses of focal lengths 4 cm and 8 cm were used to create good matching for this set of beam profile measurements (Collimator 1).

The measurements of the beam profiles can be seen in Figures 8 and 9

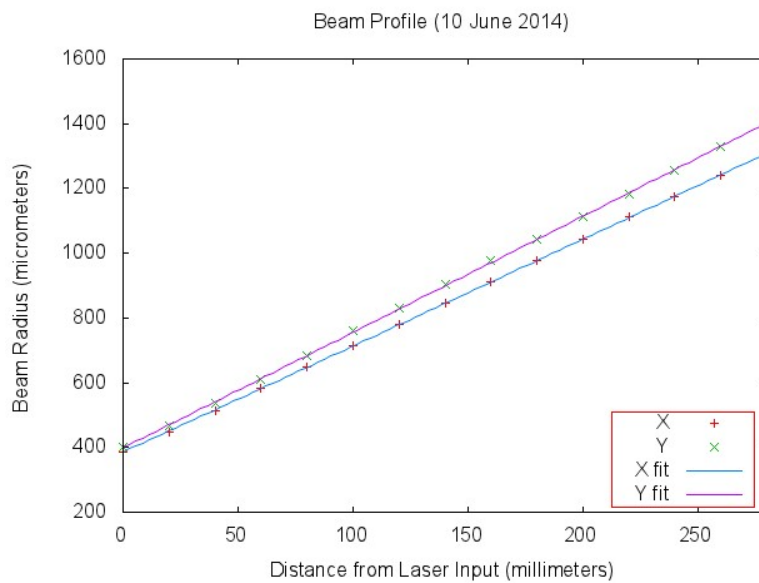


Figure 8: Beam profile of the input beam

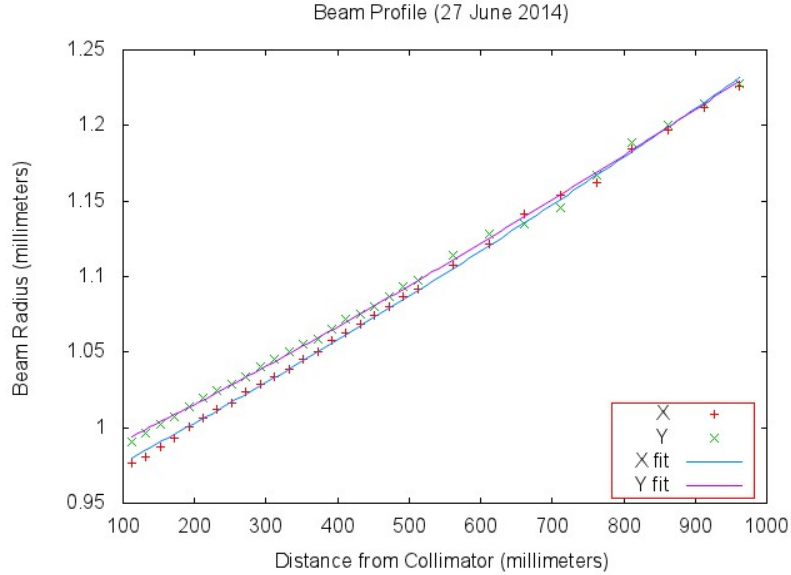


Figure 9: Beam profile of Collimator 1

In order to find the waist sizes and positions, the data were fit with the following equation [7]:

$$w(z) = w_0 \sqrt{1 + \frac{(z - z_0)^2 \lambda^2}{\pi^2 w_0^4}} \quad (6)$$

where w_0 is the waist size, z_0 is the waist position, z is the distance from z_0 and $w(z)$ is the waist size at a distance z from z_0 . The lines in Figures 8 and 9 represent these fits.

Table 1 details the waist size and position values calculated from the beam profile measurements:

Table 1: Waist Sizes and Positions

	X Waist	X Waist Position	Y Waist	Y Waist Position
Input Beam	101.7 μm	11.2 cm	93.8 μm	10.8 cm
Collimator 1	789.9 μm	124 cm	816.9 μm	125 cm

Then, by using the above measurements of the beam waist sizes and positions, along with the mode matching equations detailed above, we determined a necessary focal length of 30 cm for the lens, $d_{in} = 32.5$ cm and $d_{out} = 187$ cm. By using the measured waist positions in Table 1 the distance from the first mirror to the lens was 24.5 cm, while the distance from the lens to Collimator 1 was 62 cm. This resulted in the following final configuration for the reference beam portion of the phase camera:

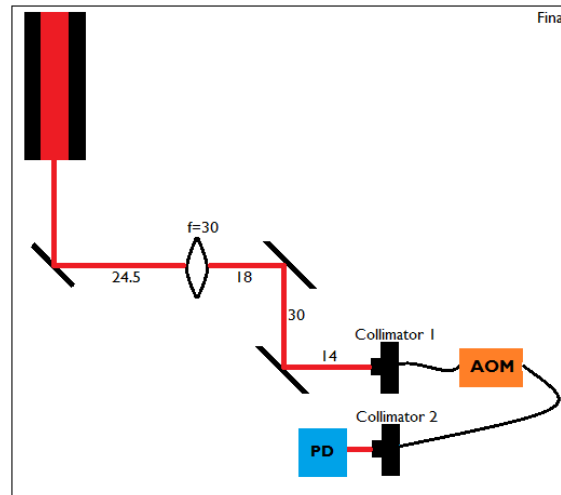


Figure 10: Final configuration for the reference beam portion of the phase camera

Once in this final configuration, slight adjustments were made to the dials, which changed the mirror positions slightly in the x and y directions. The output collimator was detected by a gain variable PD; the PD was connected to a multimeter and subsequently to a powermeter. Steady adjustment of the dials resulted in an output power value of 44 mW, 18 percent transmission, or a 25 percent increase over the initial value of 36 mW. This increase resulted from the implementation of good mode matching.

III. RF Source Optimization

The other hypothesis for the low transmission ratio was a lack of optimized RF source voltage. Initially the source voltage originated from a function generator, passed through an amplifier, then passed power to the AOM. This initial power was 3 dBm. By increasing this to the saturation point of 6 dBm, the power output at Collimator 2 increased by a factor of 3. Without the mode matching above, this optimization gives 43 percent transmission. With both mode matching and voltage optimization, the transmission was 54 percent.

However, there is still a clear discrepancy between this measured value of 54 percent and the predicted value of 63 percent. This difference is caused by the saturation point of the amplifier of 6.3 dBm. Interchanging the current amplifier with one with a slightly higher limit could increase the transmission even further.

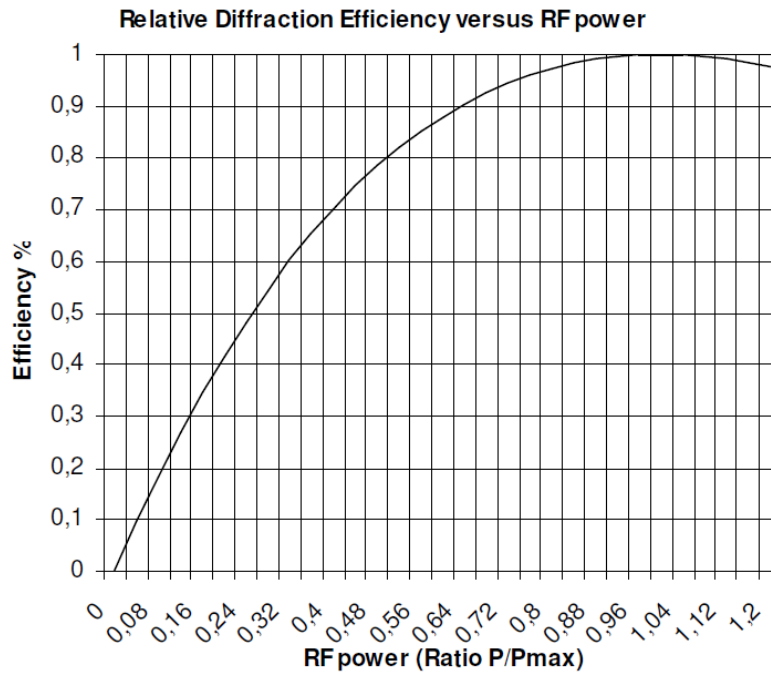


Figure 11: Transmission efficiency of the AOM vs. the normalized RF source power^[1].

IV. GOAL 2: CREATE OPTICAL LAYOUTS

The second goal of this project was to create optical layout diagrams for PC1, PC2, and PC3 to be used at the Advanced Virgo site.

I. Constraints

A successful layout is constrained by several factors. First, the size of the area available for the camera places hard limits on the positions of the components. Table 2 below shows the available space for each phase camera.

Table 2: Areas Available for Each Phase Camera

Phase Camera	Area
1	20 cm × 30 cm
2	30 cm × 90 cm
3	65 cm × 90 cm OR 30 cm × 200 cm

The size and number of components necessary for the camera is also important. In this case, a lens, beam splitter, collimator, scanner, photodetector, and a number of mirrors were required. The following table details the sizes used for each component when creating the layout:

Table 3: *Waist Sizes and Positions*

Component	Size
Lens	3 cm × 3 cm
Beam Splitter	4 cm × 4 cm
Collimator	5 cm × 5 cm
Scanner	3.5 cm × 4 cm
Photodetector	4.5 cm × 6 cm
Mirror(s)	5 cm × 5 cm

The input beam (the test beam from the interferometer) profile, the input beam waist size and position, is also relevant, and is provided by Virgo collaborators.

There are also constraints on the beam size. In order to avoid serious clipping of the beam skirts, the 99 percent criterion for passing a Gaussian beam through an aperture is used. By this criterion, stated as [7](#)

$$r = 3w \quad (7)$$

the beam size at the position of the PD must be $833 \mu\text{m}$ (radius), using a 5 mm diameter aperture. It should be noted that rounded values were often used when using this criterion. For example, for PC1, the beam size is $833 \mu\text{m}$ at a distance of 15.7 cm from the PD; however, we lack the ability to place components with such high precision. Therefore, in this case, a distance of 16 cm was used, resulting in a beam width of $844 \mu\text{m}$. This sort of approximation was used for all three layouts.

Additionally, the position of the scanner in relation to the PD is determined by the maximum tilt of the scanner, ± 25 mrad, which requires a maximum voltage. Simple trigonometry, along with the maximum tilt and the aperture size of 5 mm, dictates a minimum distance of 10 cm between the scanner and PD. However, a smaller tilt angle requires a lower voltage and allows for a higher frequency, which is preferred to create a high-density phase map. Therefore, our goal was a minimum distance of at least 20 cm, with a maximum value of 40 cm.

A final constraint was the requirement of small Rayleigh range, as compared to the distance between the beam splitter and PD. The phase camera measures the difference between the wave front of the test beam and the reference beam. The test beam should be relatively spherical, well outside the Rayleigh range, while the reference beam should be quite flat, well within the Rayleigh range. This large difference in the curvature of the test and reference beams facilitates more detailed phase maps, as can be seen in [Figure 12](#)

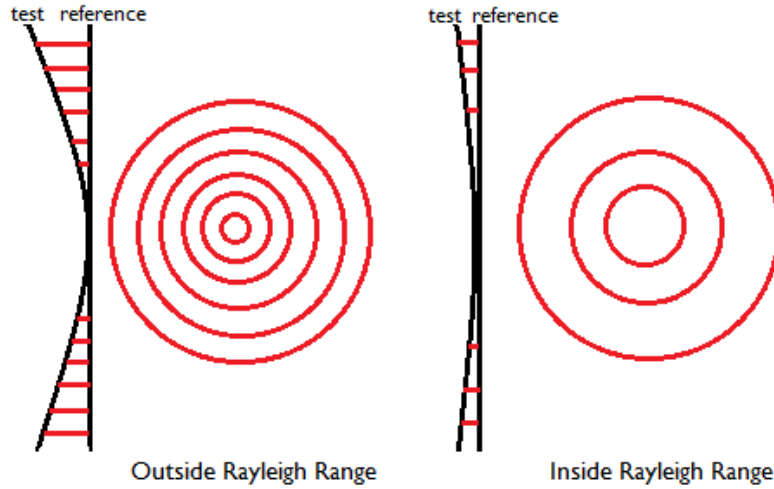


Figure 12: Difference in short vs. long Rayleigh ranges

II. Creating the Layouts

Once again, the principle of mode matching was used to determine the optimal position of the lens. The following expressions^[3] were used to determine the output waist size and position, once the input beam passed through the lens.

$$\frac{1}{w_2^2} = \frac{1}{w_1^2} \left(1 - \frac{d_1}{f}\right)^2 + \frac{1}{f^2} \left(\frac{\pi w_1}{\lambda}\right)^2 \quad (8)$$

$$d_2 - f = \frac{(d_1 - f)f^2}{(d_1 - f)^2 + \left(\frac{\pi w_1^2}{\lambda}\right)^2} \quad (9)$$

These two equations were used several times with different input waist positions and focal lengths in order to determine the best positions of the components and still remain within the constraints described above.

The final layouts can be seen in Appendix A. Creating the layout for PC1 was the most difficult, as the area available, 20 cm × 30 cm, was quite small. However, as can be seen in Figure^[13], the final distance between the scanner and PD was 23 cm, quite good for the available space.

For PC2 and PC3, it was significantly easier to include optimal scanner-PD distances, because of the larger area available. In both cases, extra reflections through mirrors were added, in order to provide more control for adjusting the input laser beam. For PC2, the optimal distance of 40 cm was able to be used because of the large area available. For PC3, a scanner-PD distance of 14 cm was used, as the Rayleigh range requirement reduced this distance.

V. CONCLUSIONS

By implementing good mode matching and optimizing the RF source voltage, we improved the transmission of the AOM by a significant amount from 14.4 percent to 54 percent. This increase will dramatically improve the signal-to-noise ratio. Additionally, we created several optical layouts for the three phase cameras, providing many options for the setups.

VI. ACKNOWLEDGEMENTS

I would first like to thank Dr. Bernard Whiting and Dr. Guido Mueller for choosing me to participate in this wonderful program, and Kristin Nichola for doing an excellent job of organizing all the logistical details. I would also like to thank my advisers Dr. Kazuhiro Agatsuma and Dr. Jo van den Brand for mentoring and challenging me this summer. I would like to thank all the members of the Gravitational Waves group at Nikhef for making me feel welcome. This program was funded by National Science Foundation Grant PHY-1005036, and I would like to acknowledge the NSF for their financial support.

REFERENCES

- [1] AOM Specifications Sheet, *AA Opto-Electronic*, 2010.
- [2] David Rabeling, K. Agatsuma, M. van Beuzekom, G. Visser, H. Verkooijen, W. Vink, and J. van den Brand. "Phase Camera Status," [slides] (11 June 2013).
- [3] Herwig Kogelnik, "Imaging of Optical Modes - Resonators with Internal Lenses," *Bell System Technical Journal*, 471 (1964).
- [4] Kazuhiro Agatsuma et al., "Phase camera development for gravitational wave detectors," [slides] (4 June 2014). Retrieved from <http://indico.cern.ch/event/192695/session/14/contribution/258> (*These proceedings will be published*).
- [5] Paul F. Goldsmith, *Quasioptical Systems*. IEEE Press, 1998.
- [6] Rudiger Paschotta, "Mode Matching," *RP Photonics*. Retrieved from http://www.rp-photonics.com/mode_matching.html.
- [7] A.E. Siegman, *Lasers*, 665 (1986).

VII. APPENDIX A

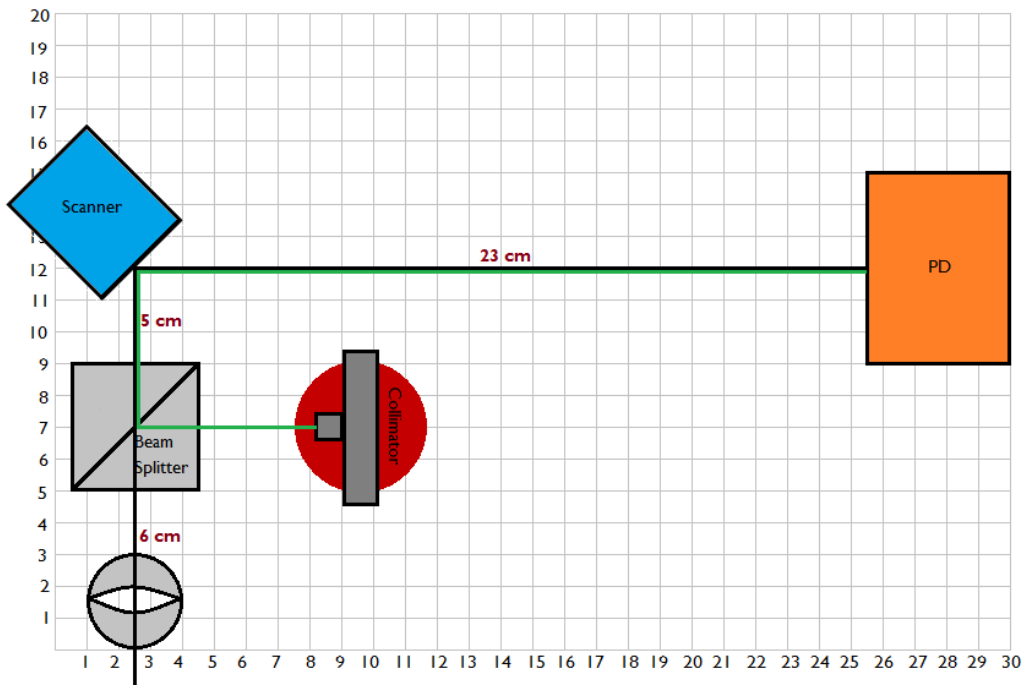


Figure 13: One of four final layouts for PC1



Figure 14: The final layout for PC2

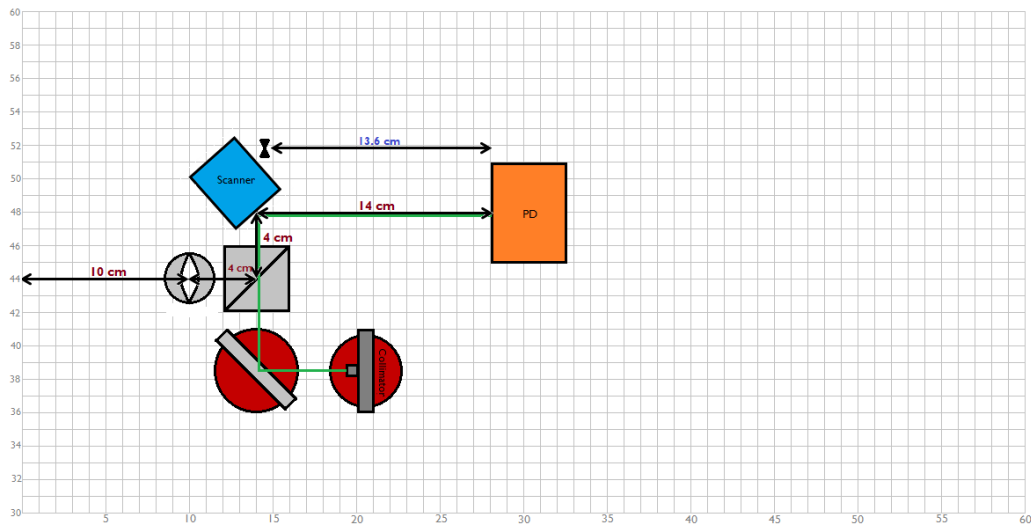


Figure 15: A preliminary layout for PC3